Nano Research

Open Access

Research Article

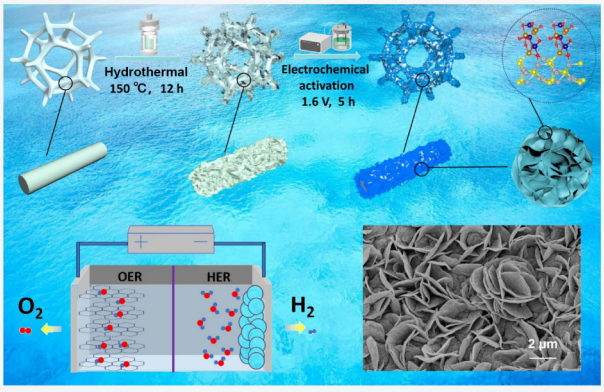
FeCo-LDH@Ni_3S_2 heterostructure with engineered d-band center for efficient oxygen evolution in alkaline electrolysis of freshwater and seawater

Wenjing Li[1,2], Xiaohong Cheng[3] ✉, Xiaoman Xiong[1] ✉, and Qi Wu[1] ✉

[1] *State Key Laboratory of New Textile Materials and Advanced Processing Technologies, Wuhan Textile University, Wuhan 430200, China*
[2] *Department of Chemistry, Yanbian University, Yanji 133002, China*
[3] *Hubei Key Laboratory of Low Dimensional Optoelectronic Materials and Devices, Hubei University of Arts and Science, Xiangyang 441053, China*

Cite this article: *Nano Research*, **2026**, *19*, 94908636. https://doi.org/10.26599/NR.2026.94908636

ABSTRACT: The search for efficient oxygen evolution reaction (OER) electrocatalysts capable of high-current-density water electrolysis is critical for scalable hydrogen production. Herein, we present a rationally designed FeCo-LDH@Ni_3S_2 heterostructure on nickel foam (NF), synthesized through a controlled approach. This electrode delivers ultralow overpotentials of 220, 235, and 245 mV at 10 mA·cm^{-2} in alkaline freshwater, simulated seawater, and natural seawater, respectively, alongside remarkable 100 h stability at industrial-level conditions (100 mA·cm^{-2} in seawater). Furthermore, a symmetric electrolyzer utilizing FeCo-LDH@Ni_3S_2 as both cathode and anode achieves low voltages of 1.60, 1.64, and 1.69 V at 10 mA·cm^{-2} in the corresponding electrolytes and exhibits over 100 h stability at 50 mA·cm^{-2}. Density-functional theory (DFT) analysis confirms that the FeCo-LDH@Ni_3S_2 heterointerface enables charge redistribution, optimizes the d-band center, and reduces the energy barrier for OER rate-determining steps. This study demonstrates an effective interface engineering strategy for d-band center reduction via heterostructure design, offering a durable electrocatalyst for marine hydrogen production.



KEYWORDS: d-band center, heterointerface, oxygen evolution reaction, interface engineering, electrocatalyst

1 Introduction

In today's world, the escalating environmental pollution and energy crisis have driven the search for green and sustainable energy sources [1–3]. Among the renewable options, hydrogen stands out due to its high energy density and clean by-products [4]. Water splitting, comprising the oxygen evolution reaction (OER) and hydrogen evolution reaction (HER), has garnered significant attention. However, the OER, with its complex multi-step electron transfer mechanism, presents greater technical challenges [5, 6]. Traditional water electrolysis relies on precious metal-based catalysts like ruthenium and platinum compounds, which are expensive and have low catalytic yields, limiting their large-scale application [7, 8]. The global water crisis further complicates matters, as high-purity freshwater is becoming scarce and costly. Seawater, making up 97% of the world's water resources, is increasingly used for large-scale hydrogen production. However, the presence of bacteria and ions such as Mg^{2+}, Ca^{2+}, and Cl^- in seawater can poison electrodes, leading to catalyst deactivation and passivation [9, 10]. In recent years, utilizing electrochemical processes for *in-situ* growth or constructing heterostructures has become an effective strategy for regulating the electronic structure of catalysts, exposing rich active interfaces, and enhancing stability. For example, Bai et al. systematically elaborated on the electrochemical C–N coupling reaction, from single step reaction to intermediate coupling, and explored strategies to improve reaction selectivity and efficiency from the design of multi active site atomic

Received: December 26, 2025; **Revised:** March 11, 2026
Accepted: March 13, 2026

✉Address correspondence to Qi Wu, wuqi2011@whu.edu.cn; Xiaoman Xiong, xmxiong@wtu.edu.cn; Xiaohong Cheng, chengxiaohong0807@126.com

level dispersed catalysts, overcoming the challenges currently faced in this field [11]. Similarly, Zhang et al. addressed the challenge of synthesizing and stabilizing multi atomic interface structures under industrial current densities by constructing atomically dispersed $Bi^0/Bi^{\delta+}$–O multi atomic interfaces in porous Bi_2O_{3-x} nanosheets, achieving efficient and stable electrocatalytic conversion of CO_2 to formate over a wide pH range [12]. These strategies have important implications for designing oxygen evolution catalysts suitable for harsh electrolysis environments. Especially for large-scale hydrogen production applications through electrolysis of water, the development of oxygen evolution catalysts that can maintain high efficiency and robustness in alkaline freshwater and even complex seawater has become a research focus. For example, Zhang et al. prepared hollow PtRuNi-O_x nanocage catalysts with ultra-low coordination structure. This catalyst exhibits outstanding performance beyond commercial Pt/C in alkaline freshwater, chemical wastewater, and seawater. Mechanism studies have shown that the ultra-low coordination structure formed by Pt, Ru, and Ni atoms, along with a large number of dangling bonds, effectively reduces the hydrolysis ionization barrier and optimizes hydrogen adsorption energy, thereby achieving precise engineering and performance breakthroughs in atomically dispersed multi metal centers [13]. The group also elaborated on the potential applications and regulatory strategies of single atom catalysts, analyzing reaction mechanisms, summarizing rational optimization methods such as ligand engineering and carrier design, and combining *in-situ* characterization and theoretical calculations to reveal the structure–activity relationship, providing forward-looking insights for promoting their large-scale applications [14].

Transition metal hydroxides, especially layered double hydroxides (LDHs), show promise as OER catalysts but are limited by sparse active sites, slow charge transfer, and low per-site efficiency [15, 16]. Constructing heterointerfaces can optimize electronic states and adsorption energies [17–21]. For instance, Sarfraz et al. epitaxially grew CuS on NiFe-LDH, achieving a heterostructure with superior HER performance [22]. Engineered interfaces can regulate metal electronics and enable novel reaction pathways, such as direct O–O bond formation, leading to performance beyond that of single-phase catalysts [23–25]. The d-band center (ε_d) connects the electronic structure to adsorbate binding energies [26]. Modulating the d-band center of Ni-based catalysts can enhance intrinsic activity and tune oxygenate adsorption [27]. Integrating $Ni(OH)_2$ with FeCo-LDH downshifts the Ni d-band center, weakening intermediate adsorption through optimized orbital interactions [24, 28]. However, experimentally controlling the electronic states of metal hydroxides remains challenging, underscoring the need for heterojunction engineering to optimize the d-band center for OER design [29–31].

Herein, we present a d-band center engineering strategy through the construction of FeCo-LDH@Ni_3S_2 heterointerfaces directly grown on nickel foam (NF) substrates. The integrated electrode demonstrates exceptional oxygen evolution performance across various electrolytes, achieving low overpotentials of 220, 235, and 245 mV at 10 mA·cm^{-2} in 1 M KOH, simulated seawater, and alkaline seawater electrolytes, respectively. Notably, the system maintains operational stability for over 100 h at industrial-level current densities (100 mA·cm^{-2}). Similarly, electrolytic cells constructed with FeCo-LDH@Ni_3S_2 as both cathode and anode (FeCo-LDH@Ni_3S_2//FeCo-LDH@Ni_3S_2) require only 1.60, 1.64, and 1.69 V to achieve 10 mA·cm^{-2} in the three solutions and maintain stability for over 100 h at 50 mA·cm^{-2}, showcasing outstanding durability under harsh electrochemical conditions. Density-functional theory (DFT) calculations reveal two fundamental electronic modulation mechanisms underlying the enhanced catalytic performance. First, interfacial charge redistribution creates localized electron accumulation, establishing optimized adsorption sites for oxygen-containing intermediates. Second, the heterojunction formation leads to a downward shift in the d-band center relative to the pristine components, fundamentally regulating intermediate binding energies. This strategic electronic configuration positions the catalyst near the apex of the OER activity volcano plot by achieving balanced adsorption–desorption thermodynamics. The shifted d-band center weakens excessive OH*/O* binding while maintaining sufficient intermediate stabilization to lower the energy barrier of the rate-determining step (RDS). The electronic synergy between metallic Ni_3S_2 and layered double hydroxide phases creates an electron-deficient interface that facilitates nucleophilic attack during water oxidation. The insights into d-band modulation and interfacial charge engineering presented here provide a universal framework for designing advanced heterostructured electrocatalysts.

2 Experimental section

2.1 Chemicals

All chemical precursors used in this water electrolysis study were obtained from certified commercial suppliers. Specifically, iron(III) chloride hexahydrate ($FeCl_3·6H_2O$, ≥ 97.0%), cobalt(II) chloride hexahydrate ($Co(NO_3)_2·6H_2O$, ≥ 97.0%), and thiourea (CH_4N_2S, ≥ 99.5%) were sourced from Sinopharm Chemical Reagent Co., Ltd. (Shanghai, China) and employed without further purification. The three-dimensional NF substrate (Tianchenghe Technology Co., Ltd., Shenzhen, China) underwent a systematic surface pretreatment. This involved sequential 10-minute ultrasonic cleaning cycles in 3 M hydrochloric acid, absolute ethanol, and deionized water. All electrochemical measurements and material preparations utilized high-purity water produced by a Millipore filtration system.

2.2 Synthesis of FeCo-LDH@Ni_3S_2

To synthesize the FeCo-LDH@Ni_3S_2 composite, 0.5 mmol of $FeCl_3·6H_2O$, 0.5 mmol of $Co(NO_3)_2·6H_2O$, and 0.5 mmol of CH_4N_2S were dissolved in 15 mL of deionized water and stirred for 30 min to ensure a homogeneous mixture. The three-dimensional NF substrate was precisely sectioned into rectangular specimens (2 cm × 3 cm) and underwent the established surface pretreatment protocol. These prepared substrates were then immersed in the precursor solution within a 25 mL Teflon-lined hydrothermal reactor. The sealed reaction vessel was maintained at 150 °C for 12 h in a temperature-controlled furnace. Following natural cooling to ambient temperature, the resulting electrocatalyst was thoroughly rinsed through multiple cycles of ethanol and deionized water to ensure complete removal of unreacted species. Final drying was accomplished in a vacuum oven at 40 °C for 12 h to obtain the desired electrode material. The resulting sample was then electrochemically activated in a 1 M KOH solution for 6 h, with a constant applied potential of 1.6 V. After 6 h of electrochemical activation, the FeCo-LDH@Ni_3S_2 catalyst was successfully obtained.

清華大学出版社 Tsinghua University Press | SciOpen

2.3 Synthesis of FeCo-LDH

Using the same hydrothermal process as described above, but without adding any sulfur source, it growed directly on NF.

2.4 Synthesis of Ni_3S_2

Using the same hydrothermal process as described above, but without adding iron and cobalt sources, vulcanization was directly carried out on NF.

2.5 Material characterization

The microstructure of the synthesized electrocatalysts was characterized by field-emission scanning electron microscopy (FE-SEM; Zeiss Sigma HD). Elemental composition was determined using energy-dispersive X-ray spectroscopy (EDS) integrated with the SEM system. Powder X-ray diffraction (XRD; Labx XRD-6100) employing Cu Kα radiation (λ = 1.5406 Å) identified the crystalline phases present. Nanoscale structural details were probed via high-resolution transmission electron microscopy (HR-TEM) conducted on a Tecnai G2 F20 microscope operating at 200 kV. Surface chemical states were assessed by X-ray photoelectron spectroscopy (XPS), with binding energies calibrated using the adventitious carbon C 1s peak at 284.8 eV.

2.6 Electrochemical measurement

Electrochemical evaluations employed a CHI 760 electrochemical workstation (Chenhua, Shanghai) configured in a standard three-electrode setup. Within this configuration, the catalyst served as the working electrode, carbon rods functioned as the counter electrode, and a Hg/HgO reference electrode was utilized. All experiments utilized a 1 M KOH aqueous solution as the electrolyte. Catalyst activity was assessed through cyclic voltammetry (CV) and polarization curve measurements, both executed at a scan rate of 5 mV·s^{-1}. Electrochemical impedance spectroscopy (EIS) spectra were acquired across a frequency range spanning 0.01 Hz to 0.1 MHz. The electrochemical surface area (ECSA) of the catalysts was evaluated from CV scans conducted at varying scan rates (10 to 50 mV·s^{-1}). Double-layer capacitance (C_{dl}) was calculated as half the slope of the linear relationship obtained from the difference in anodic and cathodic current densities. Catalyst stability was investigated via 1000 consecutive CV cycles and concurrent chronopotentiometric measurements (voltage vs. time). Notably, all electrochemical data were collected without iR compensation to ensure data integrity.

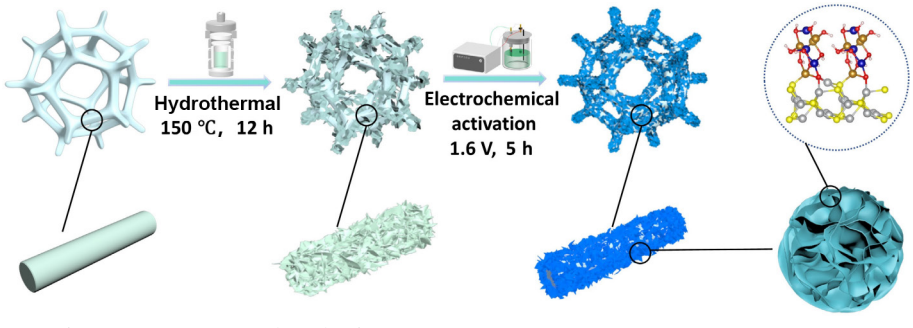
2.7 Density functional theory calculation

All DFT computations employed the Vienna *ab initio* simulation package (VASP) [32]. The Perdew–Burke–Ernzerhof (PBE) functional within the generalized gradient approximation (GGA) described electron exchange and correlation effects [33, 34]. Electron-ion interactions were modeled using the projector augmented wave (PAW) method. A plane-wave kinetic energy cutoff of 500 eV was applied. Structure relaxation of the FeCo-LDH and Ni_3S_2 heterostructure utilized a (3 × 4 × 1) k-point mesh for Brillouin zone integration, while density of states (DOS) calculations employed a (6 × 8 × 1) k-point mesh. Ionic positions were optimized towards their ground state via the conjugate-gradient algorithm. Full structural relaxation was achieved with convergence thresholds set at 1 × 10^{-6} eV for energy and 0.03 eV·Å^{-1} for forces.

3 Results and discussion

3.1 Catalysts synthesis and characterization

The synthetic strategy for catalyst fabrication is schematically depicted in Scheme 1. Hierarchical nanostructures composed of vertically aligned petal-shaped nanosheets were successfully synthesized on three-dimensional NF substrates via a controlled hydrothermal growth method, resulting in uniform spatial distribution of the active materials. Following this, the obtained precursor underwent electrochemical activation in a 1 M KOH solution at a positive voltage of 1.6 V for 6 h, resulting in the formation of FeCo-LDH@Ni_3S_2. As depicted in Fig. 1(a) and Fig. S1 in the Electronic Supplementary Material (ESM), the XRD pattern reveals distinct crystallographic features characteristic of the synthesized composite as well as individual FeCo-LDH and Ni_3S_2. The observed reflections at 21.8°, 31.1°, 37.8°, 38.3°, 49.7°, and 55.2° can be indexed to the (010), ($\bar{1}$10), (111), ($\bar{1}$11), (120), and ($\bar{1}$21) planes of the Ni_3S_2 phase (JCPDS 85-1802). Furthermore, characteristic peaks positioned at 11.6°, 23.4°, 34.1°, 38.7°, 59.1°, and 60.5° are consistent with the (003), (006), (012), (015), (110), and (113) planes of the layered double hydroxide $Co_{5.84}Fe_{2.16}(OH)_{16}(CO_3)_{1.08}{\cdot}0.32(H_2O)$ structure (JCPDS 50-0235). The morphology of FeCo-LDH@Ni_3S_2, FeCo-LDH, and Ni_3S_2 was observed by SEM. NF, as a substrate, has a smooth and porous surface, providing ample space for the growth of electrocatalysts. This surface also promotes effective gas release and helps prevent degradation of electrocatalyst performance. The morphological evolution of electrocatalysts was systematically demonstrated through single step hydrothermal and electrochemical activation synthesis. The SEM images of FeCo-LDH and Ni_3S_2 are shown in Fig. S2 in the ESM. The material is composed of interwoven nanosheets that support each other, providing a solid foundation for the stability of the catalyst, while Ni_3S_2 exhibits a particle stacking morphology. For FeCo-LDH@Ni_3S_2, it was observed that well arranged nano flower



Scheme 1 Schematic illustration of FeCo-LDH@Ni_3S_2 as anode catalyst for OER.

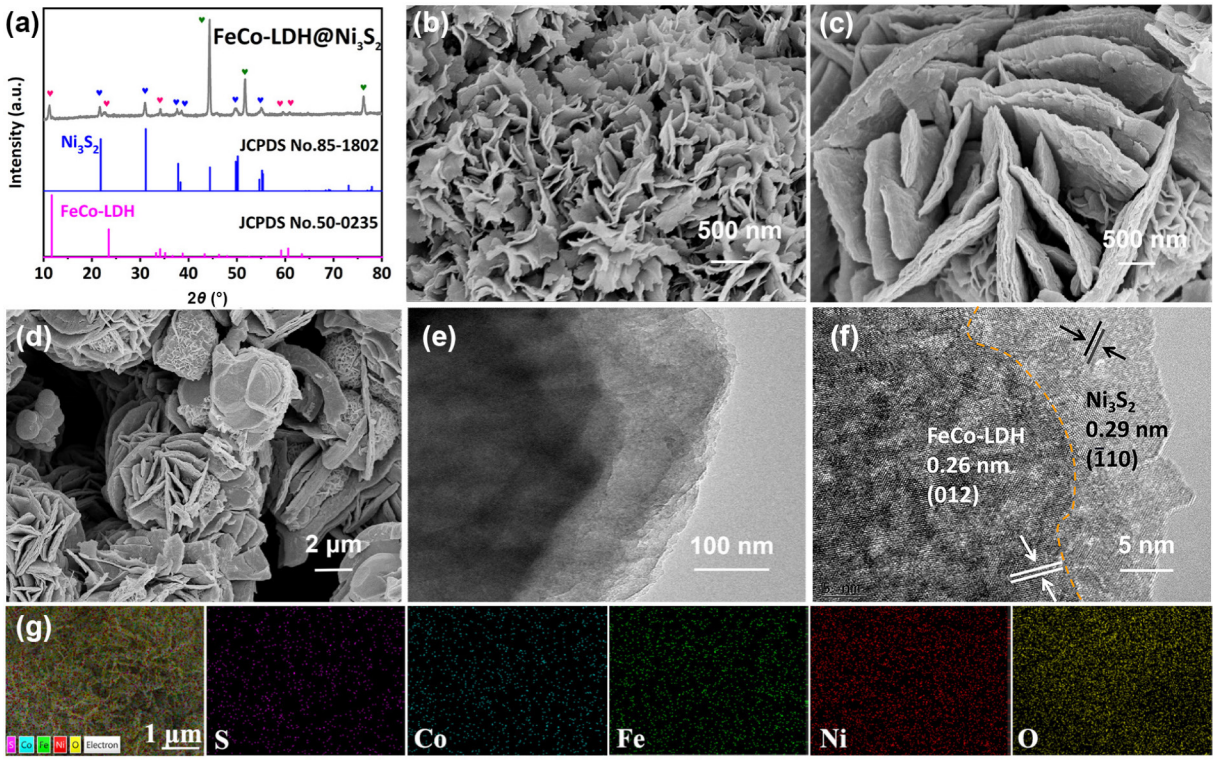


Figure 1 (a) XRD diagram. (b) Before electrochemical activation of SEM images. ((c) and (d)) After electrochemical activation of SEM images. ((e) and (f)) TEM/HRTEM diagrams, and (g) EDS element mappings of FeCo-LDH@Ni_3S_2.

structures grew vertically on the original NF substrate (Fig. 1(b)). After electrochemical activation, it clearly transformed into a three-dimensional interconnected network of nanosheets (Figs. 1(c) and 1(d)), and showed that its two-dimensional nanosheets were significantly smaller than FeCo-LDH, indicating a larger specific surface area of the structure. Compared with the initial morphology, the surface roughness and structural complexity are enhanced. This roughness phenomenon and heterogeneous nano grid structure are believed to provide a large number of active sites, providing sufficient pathways and space for electrolyte penetration and gas release. In this process, CH_4N_2S decomposes and releases S^{2-} during hydrothermal process, which reacts with the nickel atoms on the surface of foam nickel to form a nano sheet structure on the substrate surface. Subsequently, Fe^{3+} and Co^{2+} ions in the solution form the FeCo-LDH precursor under alkaline hydrothermal conditions. The abundant active sites on the Ni_3S_2 surface reduce the nucleation energy barrier of FeCo-LDH, inducing its preferential hetero-nucleation on the Ni_3S_2 surface. Then, the LDH grows into a nanosheet array along a direction perpendicular to the substrate [35, 36]. During the hydrothermal process, FeCo-LDH and Ni_3S_2 partially bond at the contact interface through strong electrostatic interactions and possible metal-sulfur bonds (Fe/Co–S), forming a tight heterointerface [37]. This interfacial coupling facilitates charge redistribution and optimizes the electronic structure. Subsequent electrochemical oxidation treatment (1.6 V vs. RHE, 1 M KOH) converts part of the LDH into more active hydroxides (such as FeCoOOH) [38]. This phase transition process is accompanied by the insertion of ions (such as OH^-) and the extraction of protons, as well as possible hydration, resulting in local lattice expansion and microscopic stress accumulation, ultimately leading to surface roughness of the catalyst. This reconstructed structure has higher mechanical stability and electrical contact, avoiding the detachment of active materials, significantly increasing the specific surface area and exposure of active sites, thereby improving the electrocatalytic performance. Further microstructural characterization through TEM analysis (Fig. 1(e)) confirms the successful formation of heterogeneous interfaces, consistent with the SEM-derived structural features. High-resolution TEM analysis provided deeper insight into the interaction between the lattice fringes of FeCo-LDH and Ni_3S_2 (Fig. 1(f)). Specifically, the plane spacing of 0.26 nm corresponds to the (012) lattice plane of FeCo-LDH, while the 0.29 nm plane spacing is attributed to the ($\bar{1}$10) lattice plane of Ni_3S_2, aligning well with the XRD results presented in Fig. 1(a). According to the selected area electron diffraction (SAED) pattern (Fig. S3 in the ESM), a series of diffraction rings reveal a polycrystalline structure, which can be attributed to the (006) and (012) crystal planes of FeCo-LDH and the ($\bar{1}$01) and ($\bar{1}$10) crystal planes of Ni_3S_2. In addition, the EDS mapping in Fig. 1(g) shows that Fe, Co, Ni, O, and S elements are present in FeCo-LDH@Ni_3S_2 uniformly dispersed within the structure. At the interface, each signal is not isolated and separated in space, but presents a tightly interwoven and interpenetrating distribution pattern. Especially at the interface of the nanosheets, obvious overlapping regions of elemental signals can be observed, which directly proves that FeCo-LDH and Ni_3S_2 have formed a tight interface contact at the nanoscale. The elemental contents and their corresponding percentages, provided in Fig. S4 in the ESM, further confirm the stable presence of these elements within the heterostructure. Collectively, these findings validate the successful synthesis of the FeCo-LDH@Ni_3S_2 heterostructure.

To gain deeper insights into the chemical states and elemental distribution within the electrocatalyst, comprehensive XPS characterization was conducted, enabling detailed analysis of both

surface composition and oxidation states. As shown in Fig. 2(a), the XPS results confirm that the FeCo-LDH@Ni_3S_2 composite is composed of Fe, Co, O, Ni, and S elements, in agreement with the EDS results shown in Fig. 1(g). To probe the valence states of the different surface atoms in greater detail, high-resolution XPS spectra of Fe 2p, Co 2p, O 1s, Ni 2p, and S 2p were analyzed, as illustrated in Figs. 2(b)–2(f). The Fe 2p spectrum (Fig. 2(b)) can be deconvoluted into several characteristic peaks. The doublets located at 711.2 eV (Fe $2p_{3/2}$) and 723.4 eV (Fe $2p_{1/2}$) are assigned to Fe^{2+}, while the features at 714.8 and 727.3 eV indicate the presence of Fe^{3+}. Additionally, a distinct peak at 706.3 eV confirms the existence of metallic Fe, and the accompanying satellite peaks complete the spectral profile [39, 40]. Co 2p speciation analysis reveals primary $2p_{3/2}$ and $2p_{1/2}$ transitions at 782.0 and 797.4 eV, respectively, characteristic of Co^{2+} species (Fig. 2(c)). The observed satellite peaks at 786.4 and 803.9 eV, along with a minor feature at 776.0 eV, suggest the co-existence of Co^{3+} [41, 42]. The O 1s spectrum (Fig. 2(d)) displays three components at 529.1, 531.6, and 532.7 eV, which are attributed to metal–oxygen bonds, hydroxyl groups, and adsorbed water molecules, respectively, confirming the complex surface chemistry [43, 44]. For the Ni species (Fig. 2(e)), the characteristic $2p_{3/2}$ and $2p_{1/2}$ transitions at 856.8 and 874.4 eV, respectively, with associated satellite features at 862.4 and 880.5 eV, confirming the presence of Ni^{2+} species [45, 46]. Finally, the S 2p spectrum (Fig. 2(f)) reveals doublet peaks at 161.1 eV (S $2p_{3/2}$) and 163.1 eV (S $2p_{1/2}$), indicative of metal–sulfur bonding, along with a higher binding energy feature at 168.5 eV, suggesting partial surface oxidation [47, 48]. This comprehensive surface analysis elucidates the complex chemical environment and oxidation states within the FeCo-LDH@Ni_3S_2 composite, providing crucial insights into its electrocatalytic properties for OER.

3.2 Electrocatalytic performance

The OER performance of the FeCo-LDH@Ni_3S_2 composite was assessed in alkaline media (1.0 M KOH) using a standard three-electrode configuration, with the synthesized material serving as the working electrode, complemented by a carbon rod counter electrode and Hg/HgO reference electrode. As shown in Fig. 3(a), the OER performance of FeCo-LDH@Ni_3S_2 was analyzed both before and after electrochemical activation. The overpotential of the catalyst decreased from 280 mV prior to activation to 220 mV post-activation, demonstrating remarkable enhancement in electrocatalytic activity. This performance improvement primarily originates from the electrochemical activation process, which generates abundant accessible active sites, optimizes charge transfer kinetics, and consequently improves the OER efficiency [49, 50]. A comparative analysis of the OER activities of FeCo-LDH@Ni_3S_2, FeCo-LDH, Ni_3S_2, NF, and RuO_2 is presented in Fig. 3(b). It is evident from the comparison that FeCo-LDH@Ni_3S_2 outperforms all other catalysts, demonstrating superior catalytic activity with an exceptionally low overpotential of 220 mV to achieve 10 mA·cm^{-2} current density, outperforming all comparative electrocatalysts. As shown in Fig. S5 in the ESM, to eliminate the influence of specific surface area on performance, the current was normalized to ECSA to verify the intrinsic activity of the catalyst. The results showed that normalized FeCo-LDH@Ni_3S_2 still exhibited higher intrinsic activity. Furthermore, the material displays remarkable reaction kinetics, as evidenced by its minimal Tafel slope of 29 mV·dec^{-1} (Fig. 3(c)), suggesting improved charge transfer kinetics. The decreased Tafel slope reflects favorable electronic structure modifications that promote efficient interfacial electron transport and enhanced mass diffusion characteristics, thereby confirming the superior OER performance of FeCo-LDH@Ni_3S_2. In contrast, FeCo-LDH (54 mV·dec^{-1}), Ni_3S_2 (78 mV·dec^{-1}), RuO_2 (83 mV·dec^{-1}), and NF (91 mV·dec^{-1}) show significantly slower reaction kinetics, which aligns with the observed OER activity trends in Fig. 3(b). Furthermore, Fig. 3(d) and Table S1 in the ESM present a clearer comparison of the overpotentials at a current density of 10 mA·cm^{-2} for various samples. It is evident that FeCo-LDH@Ni_3S_2 exhibits the best OER performance, requiring the lowest overpotential of 220 V. In comparison, other catalysts such as $Co(OH)_2$/$Ni(OH)_2$ (330 mV), $Ni(OH)_2$/$NiTe_2$ (275 mV), FeCoNi (254 mV), and MoS_2/$NiTe_2$ (275 mV) require significantly higher overpotentials. This further supports the conclusion that FeCo-LDH@Ni_3S_2

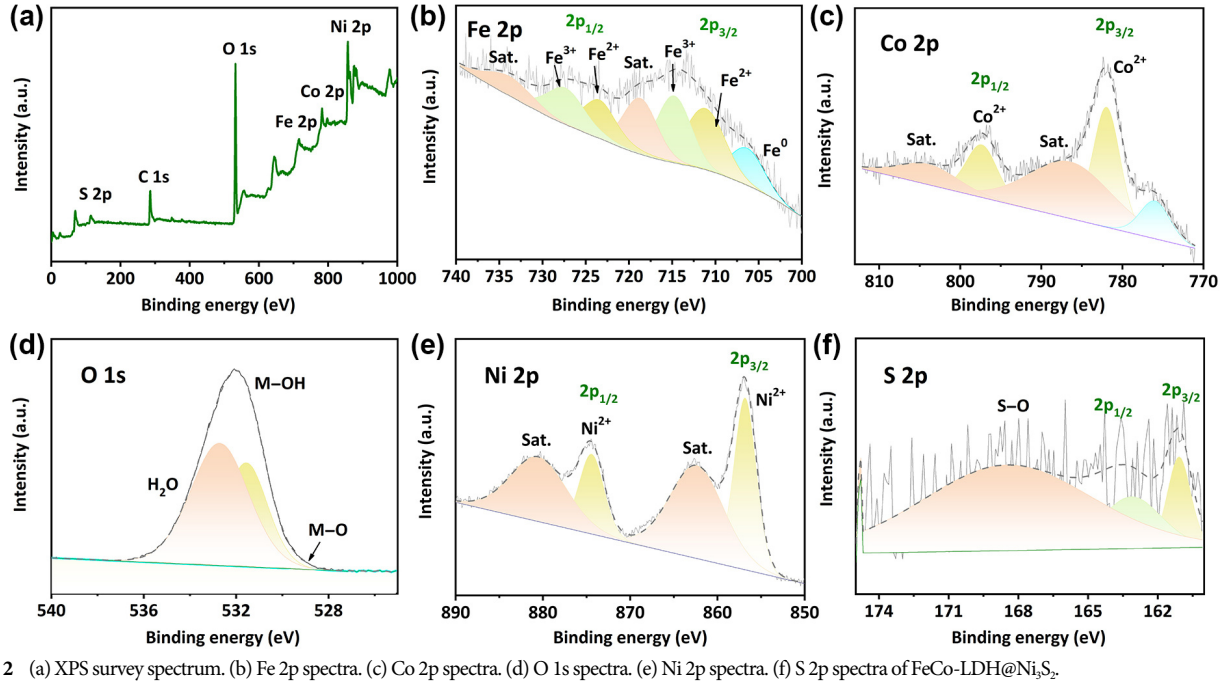


Figure 2 (a) XPS survey spectrum. (b) Fe 2p spectra. (c) Co 2p spectra. (d) O 1s spectra. (e) Ni 2p spectra. (f) S 2p spectra of FeCo-LDH@Ni_3S_2.

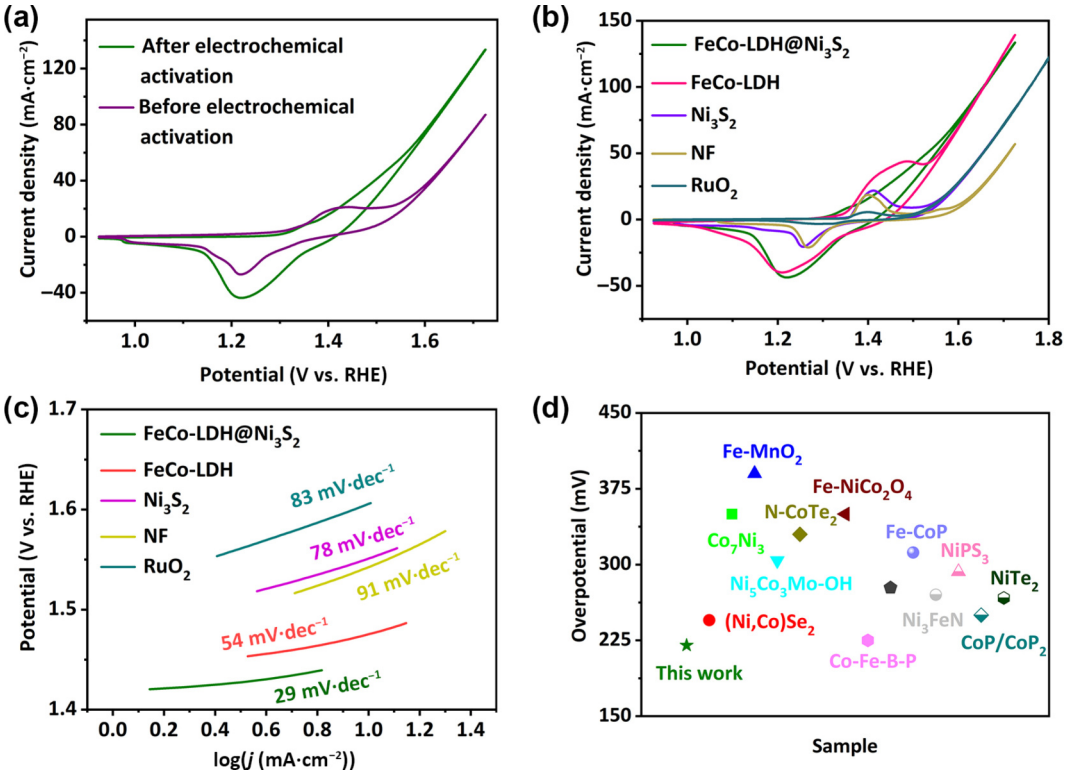


Figure 3 (a) Comparison of the OER before and after electrochemical activation of FeCo-LDH@Ni_3S_2. (b) CV curves of FeCo-LDH@Ni_3S_2, FeCo-LDH, Ni_3S_2, NF, and RuO_2. (c) Tafel slopes of FeCo-LDH@Ni_3S_2, FeCo-LDH, Ni_3S_2, NF, and RuO_2. (d) A corresponding histogram of the overpotentials of all prepared electrodes.

demonstrates superior catalytic efficiency, owing to the construction of heterostructures and the effective coupling of composite electrocatalyst nanomaterials, which substantially enhance its electrocatalytic performance. Moreover, the unique nanostructure of FeCo-LDH@Ni_3S_2, characterized by a higher density of active sites and more efficient gas flow channels, plays a pivotal role in boosting the OER activity. The enhanced electrochemical performance can thus be attributed to both the improved architecture and the synergistic effects of the FeCo-LDH and Ni_3S_2 components, which optimize the catalyst's electrocatalytic properties.

To elucidate the fundamental mechanisms responsible for the superior catalytic performance, comparative EIS measurements were systematically performed on the FeCo-LDH@Ni_3S_2 heterostructure along with its individual components (FeCo-LDH and Ni_3S_2) (Fig. 4(a)), providing deeper insights into the reaction kinetics of these electrodes. From the analysis, it is evident that FeCo-LDH@Ni_3S_2 exhibits the smallest semicircular arc, suggesting that the composite structure of the electrocatalytic materials effectively minimizes electron transfer resistance and enhances electrochemical activity. Electrochemical water splitting involves three key processes: (1) adsorption of water molecules onto the electrode surface, (2) the redox reaction of water molecules, and (3) the subsequent evolution of reaction products [51]. To understand the superior performance of the electrocatalysts, it is crucial to explore the factors that contribute to these enhanced efficiencies. The active surface area available for electrochemical reactions can be determined through C_{dl} measurements using the relationship: ECSA = C_{dl}/C_s, where C_{dl} corresponds to the electric C_{dl} and C_s represents the standard specific capacitance value, generally taken as 0.040 mF·cm^{-2} in alkaline electrolytes [38]. Figure 4(b) displays the C_{dl} values for FeCo-LDH@Ni_3S_2, FeCo-LDH, and Ni_3S_2, with FeCo-LDH@Ni_3S_2 showing a significantly larger C_{dl} (14.2 mF·cm^{-2}) compared to FeCo-LDH (9.3 mF·cm^{-2}) and Ni_3S_2 (7.0 mF·cm^{-2}). As a result, FeCo-LDH@Ni_3S_2 also demonstrates a larger ECSA than the other two catalysts, signifying that a larger ECSA correlates with enhanced electrochemical activity (Fig. S6 in the ESM). The increased number of active sites within the heterostructure and superior electrical conductivity facilitate the rate of electron transfer, ultimately improving reaction kinetics. These findings were further validated using a series of electrochemical techniques, reinforcing the relationship between the ECSA and the catalyst's overall activity. Moreover, the stability and corrosion resistance of a catalyst are essential parameters in evaluating its suitability for long-term electrocatalysis. To assess the durability of the materials, CV was performed for 1000 cycles to observe any performance degradation. As shown in Fig. 4(c), after 1000 CV cycles, the curves before and after cycling closely overlapped, with the overpotentials showing minimal attenuation. This suggests that FeCo-LDH@Ni_3S_2 possesses remarkable corrosion resistance. Furthermore, the overpotential fluctuation curves of FeCo-LDH@Ni_3S_2 at a current density of 100 mA·cm^{-2}, presented in Fig. 4(d), reveal only slight fluctuations over more than 100 h of operation, indicating excellent stability. These results confirm that FeCo-LDH@Ni_3S_2 exhibits outstanding stability in alkaline OER and fulfills the essential criteria for industrial-scale water oxidation processes.

Given that the overpotential at 10 mA·cm^{-2} is merely 220 mV, the formation of hypochlorite can be effectively suppressed [52]. These findings highlight the exceptional catalytic potential of the FeCo-LDH@Ni_3S_2 composite for saline water electrolysis applications. Comprehensive evaluation of the material's OER was conducted in two distinct alkaline electrolyte systems: imulated seawater (1.0 M KOH + 0.5 M NaCl) and natural seawater (1.0 M KOH + seawater) environments. As depicted in Fig. 5(a), FeCo-

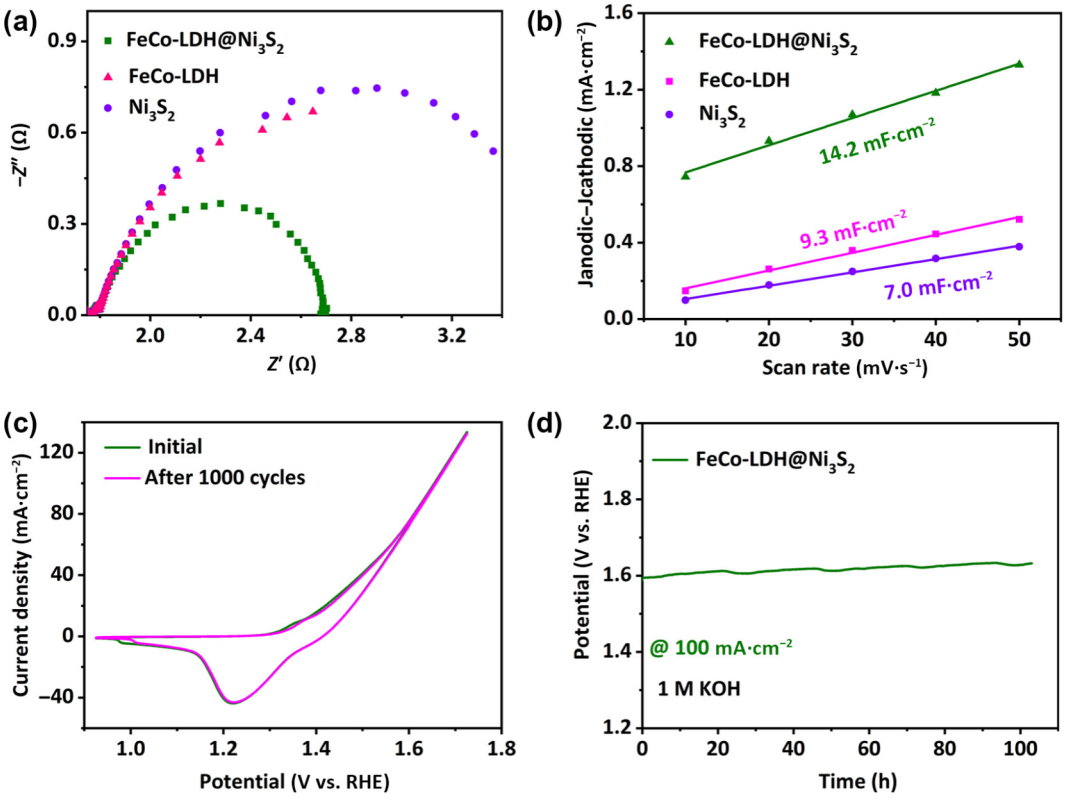


Figure 4 (a) Nyquist plots representing the electrochemical impedance spectra of FeCo-LDH@Ni_3S_2, FeCo-LDH, and Ni_3S_2. (b) C_{dl} values derived from the CV measurements of FeCo-LDH@Ni_3S_2, FeCo-LDH, and Ni_3S_2. (c) CV curves of FeCo-LDH@Ni_3S_2 before and after undergoing 1000 cycles. (d) Long-term stability assessment of FeCo-LDH@Ni_3S_2 at a current density of 100 mA·cm^{-2}.

LDH@Ni_3S_2 demonstrates robust OER activity in both environments. In the case of alkaline simulated seawater, the catalyst was capable of driving a current density of 10 mA·cm^{-2} with a remarkably low overpotential of just 235 mV. Likewise, in alkaline seawater, an overpotential of only 245 mV was required to generate the same current density, further confirming the excellent electrocatalytic performance of FeCo-LDH@Ni_3S_2. Additionally, the Tafel slope analysis reveals that FeCo-LDH@Ni_3S_2 exhibits relatively low Tafel slopes of 55 and 86 mV·dec^{-1} in simulated seawater and seawater, respectively (Fig. 5(b)), indicating superior reaction kinetics for the OER in both media. Furthermore, when comparing the activity of FeCo-LDH@Ni_3S_2 in alkaline seawater and simulated seawater with that of recently reported OER electrocatalysts (Table S2 and Fig. S3 in the ESM), it is evident that the former outperforms many of these catalysts in similar conditions. The marginal performance decrease observed in alkaline seawater electrolyte systems primarily results from active site occlusion and surface passivation induced by the adsorption of ionic species and particulate matter inherent to seawater composition [53]. Importantly, FeCo-LDH@Ni_3S_2 displayed exceptional stability, with negligible changes in overpotential over 1000 CV cycles (Figs. 5(c) and 5(d)). The composite demonstrated exceptional operational stability, maintaining a constant current output of 100 mA·cm^{-2} over an extended 100 h durability test with negligible potential fluctuation (Figs. 5(e) and 5(f)), this confirms its strong stability in KOH, simulated and natural seawater alkaline electrolytes.

The morphology, phase structure, and elemental composition of FeCo-LDH@Ni_3S_2 following stability tests were thoroughly examined using SEM, TEM, EDS, XRD, and XPS techniques, respectively. As depicted in Fig. S7 in the ESM, no notable changes were observed in the morphology of FeCo-LDH@Ni_3S_2 after the stability experiments, with the nanosheet structure being largely preserved. Moreover, the low-resolution TEM image in Fig. S8(a) in the ESM reveals that the catalyst maintains its unique nano-flake-like structure, with the flakes interconnected without significant structural collapse or agglomeration, corroborating the macroscopic morphological stability observed by SEM. In the high-resolution TEM image (Fig. S8(b) in the ESM), we can clearly observe the heterointerface between FeCo-LDH (relatively darker contrast region) and Ni_3S_2 (relatively brighter contrast region). The lattice fringes on both sides of the interface are clearly distinguishable, with a crystal plane spacing of 0.26 nm corresponding to the (012) crystal plane of FeCo-LDH, and a crystal plane spacing of 0.29 nm corresponding to the ($\bar{1}$10) crystal plane of Ni_3S_2. In addition, the HAADF-STEM image shows that darker and larger sheet-like regions correspond to FeCo-LDH nanosheets, while brighter regions represent Ni_3S_2 nanoparticles (Fig. S9(a) in the ESM). The presence and distribution of Fe, Co, O, Ni, and S elements in the material were verified by combining the corresponding element distribution maps (Fig. S9(b) in the ESM), further confirming the formation of a strong interface between FeCo LDH and Ni_3S_2. Under strong oxidation potential and alkaline conditions, no significant interdiffusion of elements or separation of interface components was observed [54, 55]. The XRD pattern shown in Fig. S10 in the ESM reveals that, after 100 h of stability testing, only a slight reduction in peak intensities was observed, likely attributed to electrochemical activation processes, while no major phase transitions occurred. The XPS analysis, presented in Fig. S11(a) in the ESM, demonstrates that the elements Fe, Co, O, Ni, and S remain detectable after the stability tests. The post-OER XPS

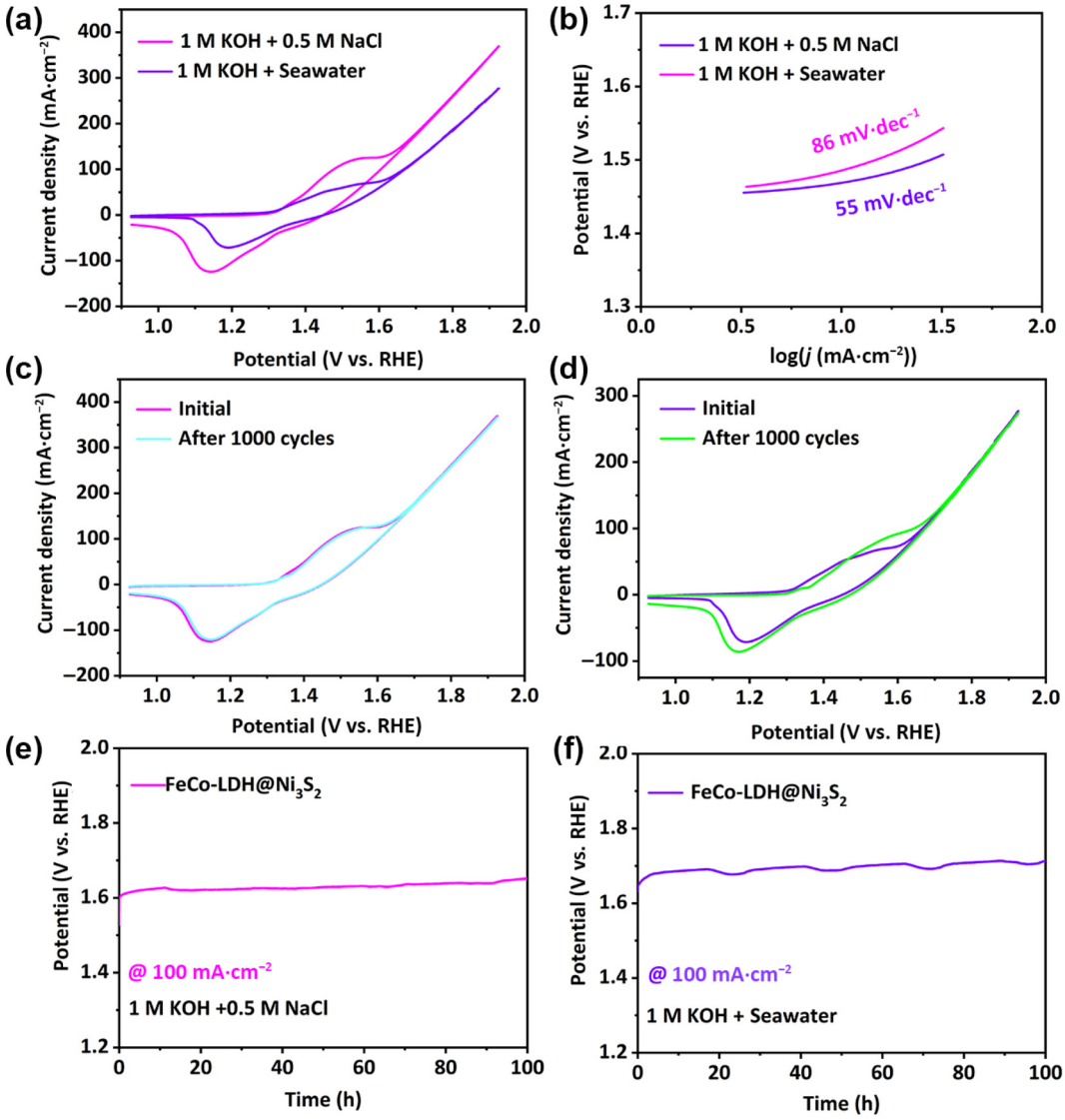


Figure 5 (a) OER polarization curves. (b) Tafel slopes. ((c) and (d)) CV curves before and after 1000 cycles and ((e) and (f)) stability test at 100 mA·cm^{-2} of FeCo-LDH@Ni_3S_2 in 1 M KOH + 0.5 M NaCl and 1 M KOH + Seawater solutions.

analysis reveals significant changes in the chemical states of surface elements. It should be pointed out that the XPS characterization of all OER samples is also a non *in-situ* test. After being removed from the electrolyte, the samples are cleaned, dried, and transferred, and the surface may come into contact with air. Although we try to shorten the transfer time as much as possible, the high valence species formed after OER may undergo partial reduction in the air, so the measured ratio may be slightly lower than the value in the real electrolysis state. However, all samples follow the same post-processing procedure, and their relative changes can still reliably reflect the valence state evolution law during the OER process. In the Fe 2p region (Fig. S11(b) in the ESM), the binding energy of Fe $2p_{3/2}$ orbitals shifts positively. Based on peak area integration calculation, the relative proportion of Fe^{3+} on the sample surface significantly increases from the initial 49.5% to 57.1%. This indicates that at the OER anode potential, the Fe species on the catalyst surface undergo rapid electrochemical oxidation, with Fe^{2+} being oxidized to Fe^{3+} species [56]. The Co 2p spectrum (Fig. S11(c) in the ESM) displays characteristic peaks at 794.7 and 779.8 eV, confirming the presence of Co^{3+} species, while the negative binding energy shift indicates the transformation from Co^{2+} to Co^{3+} during prolonged OER operation [57]. Analysis of the O 1s region (Fig. S11(d) in the ESM) demonstrates enhanced intensity of the metal–oxygen (M–O) component, consistent with the formation of a surface hydroxide layer during electrochemical testing [58]. In contrast, no significant changes were observed in the Ni 2p (Fig. S11(e) in the ESM) and S 2p (Fig. S11(f) in the ESM) spectra. In addition, XPS analysis after activation in simulated seawater and alkaline seawater showed that in the Fe 2p region (Figs. S12(a) and S12(c) in the ESM), the positive shift in binding energies for both Fe $2p_{1/2}$ and Fe $2p_{3/2}$ orbitals suggests the oxidation of Fe^{2+} to Fe^{3+} species. The Co 2p spectrum (Figs. S12(b) and S12(d) in the ESM) displays characteristic peaks at 794.5 and 780.0 eV, confirming the presence of Co^{3+} species, while the negative binding energy shift indicates the transformation from Co^{2+} to Co^{3+} during prolonged OER operation. It was confirmed that the surface of FeCo-LDH underwent electrochemical reconstruction, forming an amorphous/hydroxylated highly active surface layer. Taken together, these results suggest that FeCo-LDH@Ni_3S_2 undergoes surface activation, leading to the formation of metal hydroxides,

which are typically considered the active species in the OER process.

A two-electrode configuration was constructed for comprehensive water splitting evaluation, employing the FeCo-LDH@Ni_3S_2 composite as both anode and cathode in different electrolyte systems (Fig. 6(a)). The electrolyzer demonstrated excellent performance, achieving 10 mA·cm^{-2} at low cell voltages of 1.60, 1.64, and 1.69 V in 1.0 M KOH, alkaline simulated seawater (1.0 M KOH + 0.5 M NaCl), and natural seawater-based alkaline electrolyte (1.0 M KOH + Seawater), respectively (Fig. 6(b)). The remarkable catalytic efficiency exhibited by the FeCo-LDH@Ni_3S_2-based electrolyzer system underscores its potential as a superior bifunctional catalyst for electrochemical water decomposition, demonstrating substantial performance advantages over conventional catalytic materials reported in literature (Fig. 6(c) and Table S4 in the ESM). As the voltage increased, a considerable volume of hydrogen was visibly produced on the surface of the FeCo-LDH@Ni_3S_2 electrode, rapidly overflowing without any detachment of active material or formation of large gas bubbles (Fig. S13 in the ESM). This enhanced performance originates from the unique self-supported architecture and exceptional surface wettability characteristics of the FeCo-LDH@Ni_3S_2 composite material. Durability is a critical metric for assessing the performance of electrolyzers. The FeCo-LDH@Ni_3S_2//FeCo-LDH@Ni_3S_2 electrolyzers exhibited only a minimal decrease in the time-current curves after operating for over 100 h at a current density of 50 mA·cm^{-2} in each of the three different electrolytes (Figs. 6(d)–6(f)). This suggests that the catalyst's heterogeneous structure and synergistic effects significantly enhance stability in alkaline environments. Collectively, these results confirm the promising potential of the FeCo-LDH@Ni_3S_2 electrode for seawater electrolysis applications.

3.3 Theoretical investigation

To elucidate the synergistic interplay between FeCo-LDH and Ni_3S_2 and investigate the role of heterogeneous interfaces in the OER, we conducted systematic DFT simulations. Three distinct structural configuration—FeCo-LDH, Ni_3S_2, and their integrated heterostructure (FeCo-LDH@Ni_3S_2) were modeled (Fig. S14 in the ESM). Charge density difference analysis (Figs. 7(a) and 7(b) and Fig. S15 in the ESM) reveals pronounced electronic redistribution at the FeCo-LDH@Ni_3S_2 interface. Upon heterostructure formation, strong interfacial electronic coupling emerges, accompanied by localized charge accumulation and depletion zones, signifying substantial electron transfer across the interface. This redistributed charge density facilitates enhanced adsorption of oxygen-containing intermediates, thereby promoting catalytic activity. Figure 7(c) and Fig. S16 in the ESM systematically compare the electronic configuration evolution of FeCo-LDH@Ni_3S_2 and its individual components through projected density of states (PDOS) analysis. Theoretical calculations demonstrate that all three materials exhibit pronounced metallic characteristics, manifested through their enhanced charge transfer kinetics and superior electrical conductivity-critical properties for optimizing the reaction overpotential in oxygen evolution processes. Notably, the heterostructure formation between FeCo-LDH and Ni_3S_2 induces a significant downshift in the d-band center position relative to its parent materials. Quantitative analysis reveals d-band center values of −0.71 eV for pristine FeCo-LDH and −1.37 eV for Ni_3S_2, while the FeCo-LDH@Ni_3S_2 composite exhibits a further shifted d-band center at −1.38 eV. This electronic configuration adjustment suggests an optimized intermediate adsorption-desorption equilibrium in the hybrid material, where the moderated d-band center position corresponds to a moderate intermediate binding affinity rather than excessive adsorption strength. Based on the above calculation results, we conclude that heterostructures induce d-band center shift, charge redistribution, and ultimately affect catalytic performance [7, 59, 60]. To validate this hypothesis, thermodynamic calculations were performed under standard conditions (U = 0 V) through Gibbs free energy analysis, with corresponding optimized structural configurations along the OER pathway illustrated in Fig. 7(d) and Fig. S17 in the ESM. The potential-dependent energy profiles presented in Fig. 7(e) reveal that FeCo-LDH@Ni_3S_2 exhibits a remarkably low activation energy

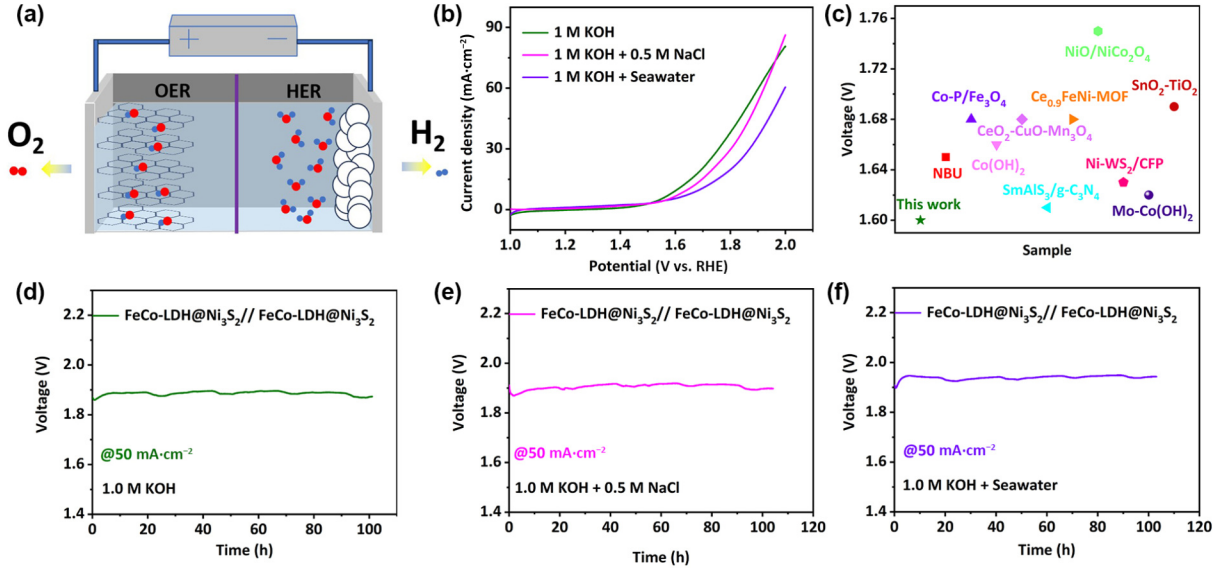


Figure 6 (a) Schematic illustration of the electrolyzer setup, where FeCo-LDH@Ni_3S_2 is employed as both the anode and cathode. (b) Polarization curves of FeCo-LDH@Ni_3S_2//FeCo-LDH@Ni_3S_2 in three different electrolytic solutions: 1 M KOH, 1 M KOH + 0.5 M NaCl, and 1 M KOH + Seawater. (c) Comparative analysis of the electrochemical performance of FeCo-LDH@Ni_3S_2//FeCo-LDH@Ni_3S_2 with relevant findings from recent research. (d)–(f) Long-term stability evaluations of FeCo-LDH@Ni_3S_2//FeCo-LDH@Ni_3S_2 in the aforementioned electrolyte solutions: 1 M KOH, 1 M KOH + 0.5 M NaCl, and 1 M KOH + Seawater.

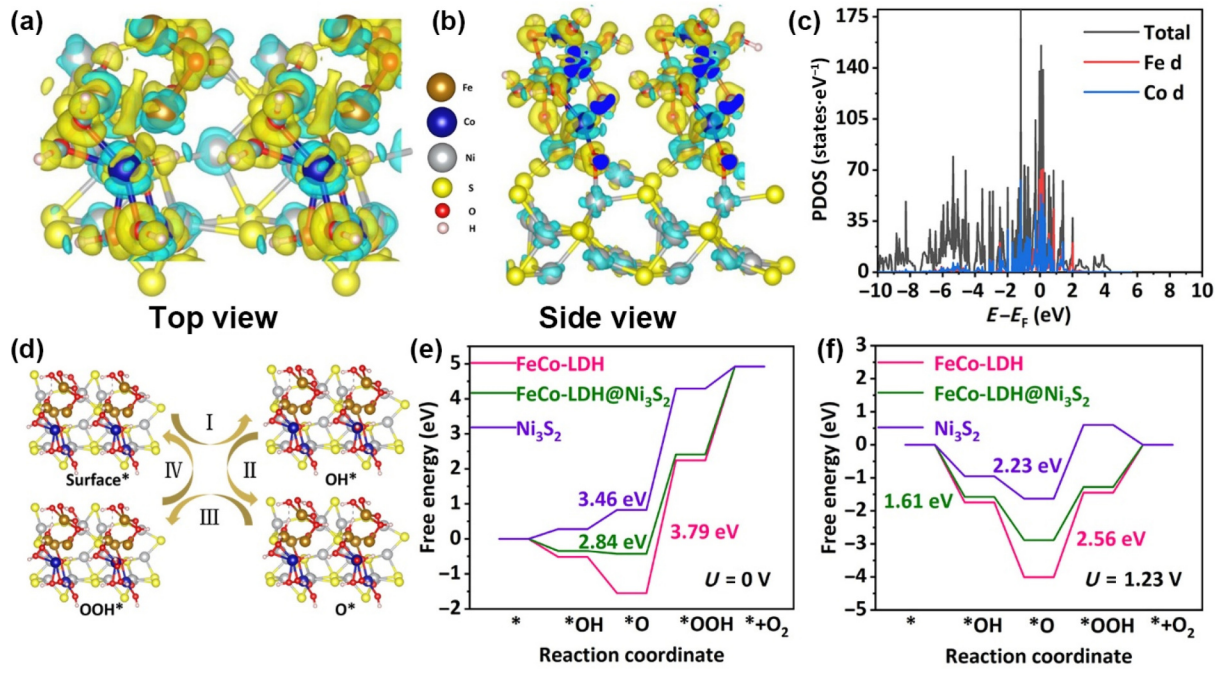


Figure 7 ((a) and (b)) Charge density differences at the FeCo-LDH@Ni_3S_2 interface. (c) Projected density of states of FeCo-LDH@Ni_3S_2. (d) Under optimized structural modeling of the basic OER four-electron reaction process with oxygen intermediates (*OH, *O, and *OOH) adsorbed at the active sites on the FeCo-LDH@Ni_3S_2 surface. ((e) and (f)) Gibbs free energy diagrams of FeCo-LDH@Ni_3S_2 in OER (U = 0 V and U = 1.23 V).

barrier of 2.84 eV for the RDS, demonstrating substantial improvement over its individual components (3.79 eV for FeCo-LDH and 3.46 eV for Ni_3S_2). Furthermore, as shown in Fig. 7(f), under applied potential conditions (U = 1.23 V), comparative analysis of RDS energy barriers follows the hierarchy: FeCo-LDH@Ni_3S_2 (1.61 eV) < Ni_3S_2 (2.23 eV) < FeCo-LDH (2.56 eV). These comparative analyses unequivocally demonstrate the superior theoretical electrocatalytic performance of the FeCo-LDH@Ni_3S_2 heterostructure. More importantly, to address concerns about the potential reconstruction of heterostructures in electrolytes, we evaluated the stability of the FeCo-LDH@Ni_3S_2 heterostructure under dynamic conditions through *ab initio* molecular dynamics (AIMD) simulations. The results showed that the total energy fluctuation of the system remained within 1 eV over 50 ps, confirming the heterostructure's excellent configurational stability and tolerance under electrochemical conditions (Fig. S18(a) in the ESM). Additionally, we calculated the energy barrier for the transformation from the hydroxide phase to the more active hydroxide oxide phase, finding that the activation barrier decreased by 0.12 eV after FeCo-LDH and Ni_3S_2 were coupled (Fig. S18(b) in the ESM). This indicates that the heterostructure significantly promotes the formation of active phases, providing a theoretical basis for understanding its structural evolution and catalytic mechanisms in real electrolyte microreaction environments. Therefore, the enhanced catalytic efficiency originates from the interfacial electronic coupling between FeCo-LDH and Ni_3S_2, which facilitates optimized adsorption energetics of water molecules and consequently reduces the activation barrier for the potential-limiting step in the OER process.

4 Conclusions

Through hydrothermal-thermochemical synthesis, we successfully constructed FeCo-LDH@Ni_3S_2 heterojunction electrocatalysts featuring vertically aligned nanosheet architecture on NF. Systematic evaluations demonstrated superior OER performance in alkaline freshwater (1.0 M KOH), simulated seawater, and natural seawater electrolytes, with low overpotentials of 220–245 mV at 10 mA·cm^{-2} and exceptional durability exceeding 100 h at 100 mA·cm^{-2}. Electrolytic cells configured with FeCo-LDH@Ni_3S_2 as both cathode and anode (FeCo-LDH@Ni_3S_2//FeCo-LDH@Ni_3S_2) achieved 10 mA·cm^{-2} current density at remarkably low voltages of 1.60, 1.64, and 1.69 V in the respective solutions and exhibited excellent stability with continuous operation for over 100 h at 50 mA·cm^{-2}. Post-operation characterization confirmed structural and elemental stability, particularly highlighting chloride-resistant corrosion mitigation in marine environments. The enhanced catalytic performance stems from heterointerface-driven electronic configuration modulation, as supported by DFT calculations. The interfacial charge redistribution between FeCo-LDH and Ni_3S_2 components induces a significant downshift in the d-band center at Ni active sites, effectively optimizing the adsorption–desorption energetics of oxygen intermediates. This electronic synergy reduces the Gibbs free energy barrier (ΔG) for the rate-determining O → OOH transition compared to monocomponent counterparts. Additionally, the electrochemical activation process exposes edge coordination-unsaturated sites, creating a self-optimized interface that sustains high activity under industrial-current-density operation. This study establishes a DFT-guided heterointerface engineering paradigm, demonstrating that atomic-level charge redistribution at transition metal compound interfaces fundamentally governs OER thermodynamics and kinetics. The d-band center manipulation strategy offers a universal framework for designing seawater-compatible electrocatalysts, effectively bridging density functional theory predictions with practical hydrogen production requirements through precisely controlled interfacial electronic structures.

Electronic Supplementary Material: Supplementary material (XRD, SEM, TEM/HTEM, XPS, DFT, more electrocatalytic test data and comparison tables) is available in the online version of this article at https://doi.org/10.26599/NR.2026.94908636.

Data availability

All data needed to support the conclusions in the paper are presented in the manuscript and the Electronic Supplementary Material. Additional data related to this paper may be requested from the corresponding author upon request.

Acknowledgements

This work is supported by the National Natural Science Foundation of China (No. 22275052) and Department of Science and Technology of Hubei Province (Nos. 2025AFA111 and 2024CSA076). The authors extend their gratitude to Ms. Liu Hong (from Scientific Compass www.shiyanjia.com) for providing invaluable assistance with the XPS analysis.

Declaration of competing interest

All the contributing authors report no conflict of interests in this work.

Author contribution statement

W. J. L.: Conceptualization, methodology, formal analysis, investigation, software, data curation, writing – original draft, writing – review & editing. X. H. C.: Formal analysis, investigation, writing – review & editing. X. M. X.: Formal analysis, investigation, writing – review & editing. Q. W.: Project administration, funding acquisition, resources, conceptualization, writing – review & editing.

Use of AI statement

None.

References

[1] Sun, Y.; Chen, Z. X.; Zhu, Z. Q.; Zheng, Y. X.; Wu, Y.; Huo, B.; Yan, F.; Wu, J. Q.; Tian, W. L. Unlocking efficient urea electrolysis: Exceptional performance of Ni_7S_6/Co_3S_4 heterostructure composites in hydrogen evolution. *Chem. Eng. J.* **2026**, *529*, 172642.

[2] Bai, H.; Yang, Y. X.; Dong, M. Y.; Yuan, H. M.; Huang, Y.; Liu, X. N.; Ni, C. Y. Structure and defect engineering synergistically boost Mo^{6+}/Mo^{4+} circulation of S_v-MoS_2 based photo-Fenton-like system for efficient levofloxacin degradation. *Appl. Catal. B: Environ.* **2024**, *358*, 124430.

[3] Bai, H.; Yang, Y. X.; Zhang, J. N.; Yang, Y. B.; Yuan, H. M.; Dong, M. Y.; Wang, C. Y.; Ni, C. Y. Modulating the redox couples of graphene-like NBC-TiO_2@FeMn through forming photo-Fenton system for boosting persulfate activation to accelerate the contaminant degradation. *Chem. Eng. J.* **2023**, *473*, 145392.

[4] Wang, J.; Li, Z.; Feng, L. B.; Lu, D. C.; Fang, W.; Zhang, Q. F.; Hedman, D.; Tong, S. F. Stable selenium nickel-iron electrocatalyst for oxygen evolution reaction in alkaline and natural seawater. *J. Colloid Interface Sci.* **2025**, *677*, 976–985.

[5] Luo, Y. X.; Yang, Y.; Tian, Y. K.; Wu, Q. S.; Lin, W. F.; Wen, M. Collaborative reconstruction of FeOOH/FeNiCo-LDH heterogeneous nanosheets for enhancing anion exchange membrane seawater electrolysis. *J. Mater. Chem. A* **2025**, *13*, 7136–7148.

[6] Wang, H.; Du, X. Q.; Zhang, X. S. Transition metal-based selenide materials derived from ZIF-67 as efficient urea and seawater splitting electrocatalyst. *Renew. Energy* **2025**, *244*, 122663.

[7] Han, W. W.; Wang, W. Y.; Liao, J. H.; He, Y.; Zhang, X. W.; Yu, C. L. Hierarchical FeCo LDH/NiSe heterostructure electrocatalysts with rich heterointerfaces for robust water splitting at an industrial-level current density. *Inorg. Chem. Front.* **2025**, *12*, 179–190.

[8] Zhang, W. C.; Li, C. E.; Sun, L.; Qian, W. C.; Yoriya, S.; He, P.; Zhu, R.; Wu, J.; Lu, Y. S.; Zeng, X. et al. Construction of Ni_3S_2@ Mo-doped CoFe-LDH electrocatalyst for oxygen evolution reaction. *J. Electroanal. Chem.* **2025**, *979*, 118931.

[9] Jian, J.; Wang, Z.; Qiao, Y.; Wang, M. T.; Nie, P.; Chang, L. M. Stainless steel mesh based $CoNiSe_4$/CoNi-layered-double-hydroxides for efficient water-splitting and durable Zn-air battery. *J. Power Sources* **2025**, *629*, 235994.

[10] Wang, F. L.; Tan, J. L.; Jin, Z. Y.; Gu, C. Y.; Lv, Q. X.; Dong, Y. W.; Lv, R. Q.; Dong, B.; Chai, Y. M. *In situ* electrochemical rapid induction of highly active γ-NiOOH species for industrial anion exchange membrane water electrolyzer. *Small* **2024**, *20*, 2310064.

[11] Bai, W. T.; Zeng, H. Y.; Chen, F. J.; Wu, S. S.; Wang, S. C.; Du, Y. P.; Liu, S. L.; Wang, D. S.; Dai, Z. H. Emerging atomistic modeling catalysts for C–N electrocatalysis. *Adv. Mater.* **2026**, *38*, e10907.

[12] Zhang, M. Y.; Zhu, W.; Liu, Z. Y.; Chen, S. R.; Zhou, D. Y.; Mu, X. Q.; Zhuang, Z. C.; Wang, S. C.; Yang, J. R.; Du, Y. P. et al. Selective sieving effect of multi-atomic bismuth interfaces for efficient formate electrosynthesis and evolution at industrial current density. *Angew. Chem.* **2025**, *137*, e202510206.

[13] Zhang, Y.; Mu, X. Q.; Liu, Z. Y.; Zhao, H. Y.; Zhuang, Z. C.; Zhang, Y. F.; Mu, S. C.; Liu, S. L.; Wang, D. S.; Dai, Z. H. Twin-distortion modulated ultra-low coordination PtRuNi-O_x catalyst for enhanced hydrogen production from chemical wastewater. *Nat. Commun.* **2024**, *15*, 10149.

[14] Zhang, Y.; Wan, W. K.; Peng, Y. D.; Guo, Y. J.; Zhou, J. L.; Wang, S. C.; Yuan, J. Y.; Liao, Y. R.; Liu, L. S.; Zhang, Y. F. et al. Corrosion-resistant single-atom catalysts for direct seawater electrolysis. *Natl. Sci. Rev.* **2025**, *12*, nwaf060.

[15] Zhang, Y. B.; Zhang, Z.; Zhang, X. X.; Li, J. S.; Guo, R. Research progress on NiCo-LDH electrocatalysts for oxygen evolution reaction. *Int. J. Hydrogen Energy* **2025**, *102*, 304–320.

[16] Mo, J. Y.; Chen, Y. W.; Guo, J.; Huang, H.; Chen, B. M.; Xu, R. D.; Guo, Z. C. Microstructure and oxygen vacancy modulation realizing high OER performance in Co-NiFe LDH. *Mater. Today Commun.* **2025**, *42*, 111162.

[17] Wu, M.; Fan, Y. Y.; Huang, Y.; Wang, D. X.; Xie, Y.; Wu, A. P.; Tian, C. G. Synergistic Ru/RuO_2 heterojunctions stabilized by carbon coating as efficient and stable bifunctional electrocatalysts for acidic overall water splitting. *Nano Res.* **2024**, *17*, 6931–6939.

[18] Cheng, R. Q.; Li, K. Q.; Li, H. X.; Sun, F. Z.; He, X. Q.; Zhao, T. S.; Zhang, J.; Fu, C. P. *In-situ* transformed Mott-Schottky heterointerface in silver/manganese oxide nanorods boosting oxygen reduction, oxygen evolution, and hydrogen evolution reactions. *Nano Res.* **2024**, *17*, 3622–3632.

[19] Zhou, W. B.; Huang, Y. C.; Cai, H. Q.; Wang, T.; Li, H. T.; Zhang, C.; Zhao, L. M.; Chen, L. L.; Liao, M. H.; Tang, Z. Q. et al. A strongly coupled cluster heterostructure with Pt–N-Mo bonding for durable and efficient H_2 evolution in anion-exchange membrane water electrolyzers. *Nano-Micro Lett.* **2025**, *17*, 296.

[20] Hu, B.; Cao, Y. Construction of an efficient CuCo-TA@FeOOH heterojunction for high-performance electrocatalytic seawater oxidation. *Front. Energy* **2025**, *19*, 757–766.

[21] Liu, Z. Y.; Chen, L. L.; Huang, S. X.; Liu, M. Q.; Ye, Q. M.; Huang, Y. C. A strongly coupled Pt–W_2N heterostructure embedded in porous carbon nanoflowers for seawater electrolysis. *Sci. China Mater.* **2025**, *68*, 3626–3637.

[22] Sarfraz, B.; Bashir, I.; Rauf, A. CuS/NiFe-LDH/NF as a bifunctional electrocatalyst for hydrogen evolution (HER) and oxygen evolution reactions (OER). *Fuel* **2023**, *337*, 127253.
[23] Israr, M.; Ali, S.; Zhang, J. Q.; Zeng, Y.; Humayun, M.; Yu, H.; Chen, X.; Chen, C.; Li, Y. D. NiFe LDH hollow nanocages confined Ru single atoms for remarkable oxygen evolution reaction. *Small* **2025**, *21*, 2500828.
[24] Guo, M. M.; Han, X. D.; Feng, H.; Chai, D. F.; Zhang, W. Z.; Li, Y.; Dong, G. H.; Guo, D. X. Spin-state-regulated dual-metal orbital engineering in heterostructured nanosheets for d-band center-optimized electrocatalytic water splitting. *J. Colloid Interface Sci.* **2025**, *696*, 137850.
[25] Li, Z. Y.; Wang, D.; Kang, H. G.; Shi, Z. N.; Hu, X. W.; Sun, H. B.; Xu, J. L. Triggering the oxide path mechanism of oxygen evolution reaction: Introducing compressive strain on NiFe-LDH by partial replacement using Ba cations. *J. Colloid Interface Sci.* **2025**, *690*, 137329.
[26] Li, C. C.; Zhang, K. N.; Wang, W. D.; Wang, Z. Q.; Yang, S. Y.; Wei, L. T.; Wang, H.; Lin, C. J.; Su, J. Z.; Guo, L. J. Synergistic yttrium doping accelerates surface reconstruction and optimizes d-band centers in NiFe-LDH for superior oxygen evolution catalysis. *J. Mater. Chem. A* **2025**, *13*, 37435–37447.
[27] Li, P. N.; Li, J. W.; Colbeau-Justin, C.; Berardan, D.; Ghazzal, M. N. Cation substitution in high-entropy layered double hydroxide driving D-band center tuning for oxygen evolution reaction. *Adv. Sci.* **2026**, *13*, e17723.
[28] Qin, T. T.; Zheng, L. J.; Pei, Z.; Wang, W. B.; Ouyang, X.; Xu, Z.; Wang, J. Z.; Guo, X. Z.; Lu, J. Electron redistribution via LDH-to-DACs coupling enhances d-band regulation and stability for zinc-air battery electrocatalysis. *ACS Nano* **2025**, *19*, 32231–32245.
[29] Xu, S.; Jiao, D. X.; Ruan, X. W.; Jin, Z. Y.; Qiu, Y.; Fan, J. C.; Zhang, L.; Zheng, W. T.; Cui, X. Q. Synergistic modulation of the d-band center in Ni_3S_2 by selenium and iron for enhanced oxygen evolution reaction (OER) and urea oxidation reaction (UOR). *J. Colloid Interface Sci.* **2024**, *671*, 46–55.
[30] Fathollahi, A.; Shahrabi, T.; Seif, A.; Du, F. H.; Li, J. Y.; Darband, G. B. A facile surface engineering approach for fabricating the superwetting Ni–Fe–Co LDH@Ni–S heterojunction as a bi-functional electrode for green hydrogen production: Experiment and theory. *J. Mater. Chem. A* **2025**, *13*, 18851–18869.
[31] Chu, C.; Li, R. C.; Chen, Q. D.; Li, W.; Li, J. W.; Jiang, S. P. Metal cations effect of Ni active sites in layered double hydroxides enables efficient anion exchange membrane water electrolysis. *J. Colloid Interface Sci.* **2026**, *703*, 139099.
[32] Kresse, G.; Furthmüller, J. Efficient iterative schemes for *ab initio* total-energy calculations using a plane-wave basis set. *Phys. Rev. B* **1996**, *54*, 11169–11186.
[33] Luo, S. J.; Zhao, Y.; Truhlar, D. G. Improved CO adsorption energies, site preferences, and surface formation energies from a meta-generalized gradient approximation exchange-correlation functional, M06-L. *J. Phys. Chem. Lett.* **2012**, *3*, 2975–2979.
[34] Perdew, J. P.; Burke, K.; Ernzerhof, M. Generalized gradient approximation made simple. *Phys. Rev. Lett.* **1996**, *77*, 3865–3868.
[35] Duan, J. J.; Han, Z.; Zhang, R. L.; Feng, J. J.; Zhang, L.; Zhang, Q. L.; Wang, A. J. Iron, manganese co-doped Ni_3S_2 nanoflowers *in situ* assembled by ultrathin nanosheets as a robust electrocatalyst for oxygen evolution reaction. *J. Colloid Interface Sci.* **2021**, *588*, 248–256.
[36] Du, X. Q.; Yang, Z.; Li, Y.; Gong, Y. Q.; Zhao, M. Controlled synthesis of $Ni(OH)_2/Ni_3S_2$ hybrid nanosheet arrays as highly active and stable electrocatalysts for water splitting. *J. Mater. Chem. A* **2018**, *6*, 6938–6946.
[37] Li, W. J.; Yue, J. Q.; Yin, C. R.; Yin, Z. X. S-doping engineering of $Fe_2O_3/NiTe_2$ heterostructures for electronic structure tuning to promote efficient urea oxidation. *J. Colloid Interface Sci.* **2026**, *706*, 139647.
[38] Mei, J.; Deng, Y. Q.; Cheng, X. H.; Wu, Q. Facile and scalable synthesis of Ni_3S_2/Fe_3O_4 nanoblocks as an efficient and stable electrocatalyst for oxygen evolution reaction. *J. Colloid Interface Sci.* **2024**, *660*, 440–448.
[39] Xu, S. R.; Yu, X.; Luo, L.; Li, W. J.; Du, Y. S.; Kong, Q. Q.; Wu, Q. Multiscale manipulating induced flexible heterogeneous V-$NiFe_2O_4$@Ni_2P electrocatalyst for efficient and durable oxygen evolution reaction. *Nano Res.* **2022**, *15*, 4942–4949.
[40] Srinivas, K.; Chen, Y. F.; Wang, B.; Yu, B.; Wang, X. Q.; Hu, Y.; Lu, Y. J.; Li, W. X.; Zhang, W. L.; Yang, D. X. Metal-organic framework-derived NiS/Fe_3O_4 heterostructure-decorated carbon nanotubes as highly efficient and durable electrocatalysts for oxygen evolution reaction. *ACS Appl. Mater. Interfaces* **2020**, *12*, 31552–31563.
[41] Yang, X.; Cheng, J.; Xu, Y.; Li, H.; Tu, W. F.; Zhou, J. H. Heterogeneous ultra-thin FeCo-LDH@ $Co(OH)_2$ nanosheets facilitated electrons transfer for oxygen evolution reaction. *Chem. Eng. J.* **2023**, *472*, 145076.
[42] Cai, C.; Hao, L.; Sun, D. H.; Chen, Z. T.; Yan, H. Y.; Zhang, Y. F. Novel *N*-doped biomass carbon spheres loaded with *In-Situ* grown FeCo layered double hydroxide for oxygen evolution reaction. *J. Colloid Interface Sci.* **2025**, *680*, 356–364.
[43] Deng, X.; Chen, J. W.; Chen, Q. Y.; Zhou, Y. Z.; Liu, X. C.; Zhang, J.; Wang, G.; Wang, R. L. The synergistic effect of Ir and oxygen vacancies on Enhancing the OER performance of Surface-Reconstructed FeCo LDH. *Appl. Surf. Sci.* **2024**, *665*, 160310.
[44] Zhou, J. J.; Liang, J. H.; Fan, Z. H.; Tan, W. J.; Sun, X. J.; Ding, R.; Gao, P.; Zhang, Y. W. $NiFe_2O_4/Ni_2P$ Mott-Schottky heterojunction boosts the oxygen evolution reaction in alkaline water/natural seawater. *Int. J. Hydrogen Energy* **2024**, *51*, 770–778.
[45] Li, W. J.; Yu, X.; Luo, L.; Du, Y. S.; Wu, Q. Fe-doped $NiTe_2/Ni_2P$ grown *in situ* on Ni foam as an efficient electrocatalyst for oxygen evolution reaction. *J. Alloys Compd.* **2022**, *917*, 165369.
[46] Li, W. J.; Deng, Y. Q.; Luo, L.; Du, Y. S.; Cheng, X. H.; Wu, Q. Nitrogen-doped $Fe_2O_3/NiTe_2$ as an excellent bifunctional electrocatalyst for overall water splitting. *J. Colloid Interface Sci.* **2023**, *639*, 416–423.
[47] Tong, R.; Xu, M.; Huang, H. M.; Wu, C. R.; Luo, X.; Cao, M. L.; Li, X. X.; Hu, X. S.; Wang, S. P.; Pan, H. 3D V–Ni_3S_2@CoFe-LDH core-shell electrocatalysts for efficient water oxidation. *Int. J. Hydrogen Energy* **2021**, *46*, 39636–39644.
[48] Mu, J. S.; Peng, A. Z.; Wang, X. R.; Wang, J.; Hong, Z. J.; Guo, D. N.; Lei, S. L.; Wang, J. J.; Yang, E. C. Morphology and structural regulation of S and Cr Co-doped FeOOH nanoarray for promoting oxygen evolution reaction. *ACS Appl. Nano Mater.* **2024**, *7*, 14005–14015.
[49] Seenivasan, S.; Seo, J. Inverting destructive electrochemical reconstruction of niobium nitride catalyst to construct highly efficient HER/OER catalyst. *Chem. Eng. J.* **2023**, *454*, 140558.
[50] Esquius, J. R.; González-Ingelmo, M.; García, M. L.; Laruelo, A. V.; Santamaría, R.; Blanco, C.; Rocha, V. G. Self-supported $FeCoNi(OH_y)O_x$ oxy-hydroxide doped with Cr and Cu as robust low-loading catalyst for the alkaline oxygen evolution reaction. *Int. J. Hydrogen Energy* **2025**, *142*, 596–605.
[51] Jiang, J.; Zhang, A. L.; Li, L. L.; Ai, L. H. Nickel-cobalt layered double hydroxide nanosheets as high-performance electrocatalyst for oxygen evolution reaction. *J. Power Sources* **2015**, *278*, 445–451.
[52] Li, Y. X.; Zhang, Z.; Zhang, Z. Q.; He, J. H.; Xie, M. G.; Li, C. G.; Lu, H. Y.; Shi, Z.; Feng, S. H. Construction of Ni_2P-$NiFe_2O_4$ heterostructured nanosheets towards performance-enhanced water oxidation reaction. *Appl. Catal. B: Environ.* **2023**, *339*, 123141.
[53] Ge, S. Y.; Shen, X. R.; Gao, J. X.; Ma, K. X.; Zhao, H. Y.; Fu, R. R.; Feng, C. H.; Zhao, Y.; Jiao, Q. Z.; Li, H. S. Synergy of Mo doping

and heterostructures in $FeCo_2S_4$@Mo-NiCo LDH/NF as durable and corrosion-resistance bifunctional electrocatalyst towards seawater electrolysis at industrial current density. *Chem. Eng. J.* **2024**, *485*, 150161.

[54] Guan, Z.; Chen, H. Z.; Chen, B.; Kong, L. C.; Shi, Z.; Zhong, Y.; Li, W. J.; Qian, W. C.; Zhang, R.; Wu, J. et al. Interfacial electron modulation of FeCo LDH@CoS heterojunction for efficient oxygen evolution reaction. *J. Environ. Chem. Eng.* **2025**, *13*, 118407.

[55] Singha Roy, S.; Madhu, R.; Bera, K.; Nagappan, S.; Dhandapani, H. N.; De, A.; Kundu, S. Tuning the activity and stability of CoCr-LDH by forming a heterostructure on surface-oxidized nickel foam for enhanced water-splitting performance. *ACS Appl. Mater. Interfaces* **2024**, *16*, 5965–5976.

[56] Jia, L. N.; Du, G. H.; Han, D.; Wang, Y. T.; Zhao, W. Q.; Su, Q. M.; Ding, S. K.; Xu, B. S. Magnetic electrode configuration with polypyrrole-wrapped Ni/$NiFe_2O_4$ core–shell nanospheres to boost electrocatalytic water splitting. *Chem. Eng. J.* **2023**, *454*, 140278.

[57] Li, S. S.; Qiu, X. Z.; An, X. W.; Li, E. Z.; Li, X. Y.; Wang, G. R.; Li, P.; Shi, C. X.; Liu, Y. M.; Guan, G. Q. Metal-organic framework derived spinel tricobalt tetroxide with trifle iridium sites for near-pH-neutral seawater electrolysis. *Chem. Eng. J.* **2024**, *491*, 151924.

[58] Zhang, H. M.; Gao, Y. H.; Li, J. K.; Sun, J. F.; Wang, D. L.; Wang, L. W.; Meng, Y. Q. Enhancing electronic communication in amorphous-crystalline NiCoS-CeO_x heterostructure for efficient overall water/simulated seawater electrolysis. *Fuel* **2024**, *375*, 132652.

[59] Xu, X. C.; Liao, H. J.; Huang, L.; Chen, S. J.; Wang, R.; Wu, S.; Wu, Y. X.; Sun, Z. P.; Huang, H. T. Surface reconstruction and directed electron transport in $NiSe_2$/$MoSe_2$ Mott–Schottky heterojunction catalysts promote urea-assisted water splitting. *App. Catal. B: Environ.* **2024**, *341*, 123312.

[60] Li, W. J.; Hu, A. R.; Liu, L. R.; Han, S. Y.; Yin, Z. X. 3D Co-doped $NiFe_2O_4$/$NiTe_2$ nanoblocks electrocatalyst enables efficient oxygen evolution reactions in alkaline freshwater and seawater. *Mater. Today Chem.* **2025**, *47*, 102840.

This is an open access article under the terms of the Creative Commons Attribution 4.0 International License (CC BY 4.0, https://creativecommons.org/licenses/by/4.0/).

© The Author(s) 2026. Published by Tsinghua University Press.